Human Sleep Posture Recognition Method Based on Interactive Learning of Ultra-Long Short-Term Information

Bing Luo, Zhaocheng Yang, *Member, IEEE*, Ping Chu, and Jianhua Zhou

***Abstract*—The sleep posture recognition and tracking using radar sensor is one of the most important techniques because of its advantages of stable performance, privacy protection, and so on. However, radar echo signals are highly sensitive to different humans, resulting in a week generalization ability. To solve this problem, we propose a human sleep posture recognition method based on interactive learning of ultra-long short-term information using millimeter-wave radar. The motivation of the proposed method using the interactive learning strategy lies that it is easy to obtain stable information with an ultra-long-term observation. Specifically, we first conduct short-term human state separation sequentially by body movement index estimation, big movement detection, range–Doppler map calculation, and lateral and nonlateral rough identification. This could separate the three human states of big movement, lateral posture, and other recumbency, and prepare for finer posture recognition. Second, we sort the three sleep postures of supine, side, and prone and extract personalized features with an ultra-long-term observation to enhance the robustness. Finally, combined with the extracted personalized ultra-long-term features, we achieve recognition of three sleep postures and seven sleep postural conversions (SPCs) with a short-term observation for real-time judgment. The experimental results show that the proposed method has low computational complexity and can achieve an average accuracy of 91% in three sleep postures' recognition and 83.7% in seven SPCs' classification.**

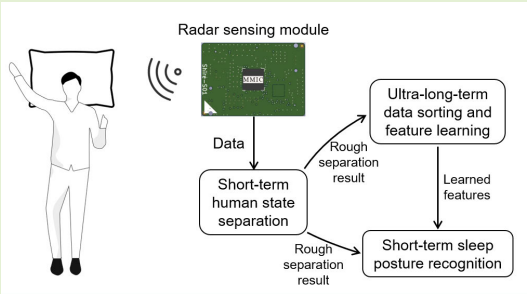

***Index Terms*—Interactive learning, millimeter-wave radar, sleep posture recognition, ultralong short-term information.**

I. Introduction

With the development of social economy, people pay more and more attention to their health status, with strong demand for health monitoring system. Sleep posture is not only closely related to physical condition but also an important component for sleep assessment. Studies have shown that the supine posture is consistently associated with obstructive sleep apnea (OSA) for adults [1], and the increase in the number and severity of apnea events was observed in supine posture [2]. Nevertheless, sleeping in lateral posture can effectively improve this problem [3]. Moreover, prone posture remains one of the most significant risk factors for sudden infant death syndrome (SIDS) because of the effects on respiration caused by pressure on the chest [4]. In addition, for bedridden patients, maintaining the same posture for a long time can lead to ulcers and bedsores. By regularly adjusting the patient's sleep posture, the nurses can effectively prevent pressure sores. Therefore, it is of great significance to recognize and track human sleep postures.

The sensors currently used for sleep posture recognition can be divided into two categories: contact and noncontact. Contact sleep posture recognition sensors are mainly accelerometer sensors and pressure sensors. Chang and Liu [5] and Yoon et al. [6] wore accelerometer on the chest to detect sleep posture, while Borazio and Laerhoven [7] used a wrist-worn sensor to record the 3-D acceleration. However, the installation way seriously influences sleep quality. Also, the pressure sensors can recognize different sleeping postures according to the pressure distribution of human body with different sleep postures [8], [9]. However, it is easy to exceed the detection range and the hardware cost is expensive. Noncontact

Manuscript received 12 March 2023; revised 19 April 2023; accepted 21 April 2023. Date of publication 11 May 2023; date of current version 14 June 2023. This work was supported in part by the Science and Technology Project of Shenzhen under Grant JCYJ20190808142803565, in part by the Guangdong Basic and Applied Basic Research Foundation under Grant 2022A1515140014, and in part by the National Natural Science Foundation of China under Grant 62101207. The associate editor coordinating the review of this article and approving it for publication was Dr. Ravibabu Mulaveesala. *(Corresponding author: Zhaocheng Yang.)*

The authors are with the State Key Laboratory of Radio Frequency Heterogeneous Integration, College of Electronics and Information Engineering, Shenzhen University, Shenzhen 518060, China (e-mail: 2017133046@email.szu.edu.cn; yangzhaocheng@szu.edu.cn; chuping@szu.edu.cn; zhoujianhua45@szu.edu.cn).

Digital Object Identifier 10.1109/JSEN.2023.3273533

sleep posture recognition sensors include visual sensors, WI-FI sensors, and radar sensors. The visual sensors mainly rely on the acquired high-resolution images or videos. It can not only monitor the sleep posture [10], [11] but also estimate the respiratory rate and detect the apnea event [12]. However, high computational cost, sensitivity to the light, covering of clothes and quilts, and privacy concerns limit the application of vision sensors [10], [11], [12], [13], [14]. As for WI-FI sensors, Yang et al. [15] estimated the human respiration rate by extracting the channel state information (CSI). Extracting features from channel frequency response (CFR) sequence can also realize the classification of different sleep postures [16], [17], [18]. However, WI-FI signals are very sensitive to the environment. What is more, the flow of WI-FI depends on the real-time needs of users or the Internet-of-Things (IoT) devices and cannot be manually controlled in practical applications.

There are advantages of stable performance, privacy protection, and not being affected by covering of clothes and quilts for radar sensors. Hence, many scholars have applied it to the recognition of sleep postures. Currently, there are primarily three strategies for radar-based sleep posture recognition: traditional detection techniques (TDTs) [20], [21], traditional machine learning (TML) [22], [23], [24], [25], [26], and deep neural networks (DNNs) [26], [27], [28], [29], [30], [31]. Kiriazi et al. [19] conducted thorough research on the radar cross section (RCS) and the displacement of the thoracic movement for different sleep postures. Then, they proposed a dual-frequency decision algorithm based on two radars for sleep posture recognition, with the accuracy of 90%, 80%, and 100% for 2.4 GHz, 5.8 GHz, and dual-frequency radar, respectively [20]. More finely, Nguyen et al. [21] tried to estimate the angle between the human's body and the bed surface based on the gradient change of the vital signal. What is more, there are many TML methods applied on sleep posture detection. Based on the research in [19] and [20], Islam et al. used three TML methods, i.e., K-nearest neighbor (KNN), support vector machine (SVM), and decision tree (DT), to identify sleep postures [22]. Also, the accuracy is 85%, 85%, and 98.4% for 2.4 GHz, 5.8 GHz, and dual-frequency radar, respectively. Nguyen et al. [23] extracted multiple time- and frequency-domain features from the echo signal and applied KNN to classify supine, left, and right posture. Higashi et al. [24] applied the multinomial logistic regression (MNR) to recognize five human states: supine, lateral, prone, moving, and leaving with an accuracy of 88.5%. Lai et al. [26] installed radars above the bed and on the side of the bed. They applied the TML and DNN to recognize supine, left, right, and prone posture. Also, the results show that the DNN did not necessarily perform better and even worse than the TML method because of the lack of large dataset. Normally, DNN methods require large-scale labeled data to prevent overfitting and obtain good generalization [27]. Zheng et al. [28] proposed an unsupervised human contour extraction method for through-wall radar (TWR) images. Moreover, Yue et al. [29] transferred the learning model to adapt to a specific human in a new environment. Zheng et al. [30] recovered the pose and shape of the human body from TWR images. Piriyajitakonkij et al. [31] first proposed a sleep postural conversion (SPC) recognition model based on ultrawideband (UWB) radar. Based on the multiview learning (MVL) and deep convolution neural network (DCNN), they classified four SPC categories with a mean accuracy of 73.7% ± 0.8%, including supine to lateral (SULA), supine to prone (SUPR), lateral to supine (LASU), and prone to supine (PRSU).

Although a number of radar-based methods have been proposed for sleep posture recognition, there are still three main challenges: 1) scholars pay little attention to SPC among the above studies; 2) we need to reduce the computational complexity of the method in order to perform edge computing; and 3) sleeping posture recognition method has weak generalization ability because of the high sensitivity of radar echo signals. To solve the above problems, we propose a human sleep posture recognition method based on interactive learning of ultra-long short-term information (IL-ULSTI). The core idea of the proposed method lies in improving the generalization ability for different humans through interactive learning. Specifically, we first perform a detailed analysis of the range–Doppler (RD) map of different postures and separate various human states through the detection of big movement and the rough identification of lateral and nonlateral. Next, in order to improve the robustness of the method for different humans, we sort the three sleep postures of supine, side, and prone and extract the personalized features with an ultra-long-term observation. Finally, combined with the extracted personalized ultra-long-term features, we achieve recognition of three sleep postures and seven SPC categories with a short-term observation for real-time judgment. After exhaustive experiments and analysis, it is proved that our method can effectively enhance the robustness to different humans through interactive learning. Moreover, since the DNN is not utilized, the computational complexity is relatively more suitable for edge devices.

The rest of this article is organized as follows. Section II describes the signal model of the radar. In Section III, the proposed IL-ULSTI-based sleep posture recognition method is detailed. Section IV discusses the experiment results to demonstrate the effectiveness of the proposed method. Finally, the conclusions will be drawn in Section V.

II. Signal Model

The considered sensor is a 60-GHz millimeter-wave single-input–single-output (SISO) radar module with 6.8-GHz continuous bandwidth. The transmitted signal from transmitter is expressed as

$$s(t,m) = A_T e^{-j\left\{2\pi\left[f_c(mT_p+t)+\frac{Bt^2}{2T_c}\right]+\phi_0\right\}} \tag{1}$$

where A_T is the amplitude of transmitted signal, f_c represents the carrier frequency, $m = 0, 1, \ldots, M-1$ is the chirp index, M is the number of the chirps, T_p is the sampling interval at the slow time, T_c is the pulsewidth of a chirp, $t \epsilon [0, T_c]$ is the fast time within a chirp, B is the bandwidth, B/T_c represents the changing rate of the signal frequency, and ϕ_0 is the initial random phase generated by the oscillator. The received signal

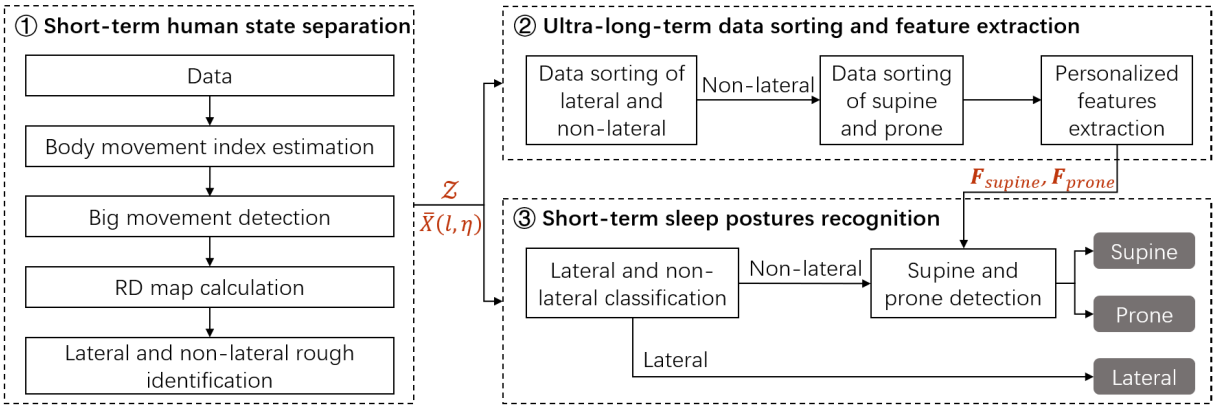

Fig. 1. Proposed sleep posture recognition method.

for a short-range observation can be given by

$$\bar{y}(t,m) = \sum_{k=1}^{K} \bar{\rho}_k s\,(t-\tau_k, m) + \bar{y}_u(t,m) + \bar{y}_n(t,m) \quad (2)$$

where K is the number of human body scatterers, $\bar{\rho}_k$ is the received signal amplitude of the kth scatterer, $\tau_k = (2[R_k + v_k(mT_p + t)])/c$ denotes the time delay of the kth scatterer, R_k and v_k are the initial distance and radial velocity between the kth scatterer and the radar antenna, respectively, c is the velocity of light, $\bar{y}_u(t,m)$ is the clutter signal, and $\bar{y}_n(t,m)$ is the white noise.

In practical application scenarios, $(B\tau_k^2)/(2T_c)$ tends to zero and can be ignored since τ_k is small. When human is stationary, the radial velocity of each scatterer is so small that $(2v_k t)/\lambda$ can be neglected. After dechirp operation and analog-to-digital conversion, the received signal can be approximated as

$$y(n,m) \approx \sum_{k=1}^{K} \rho_k e^{j4\pi\left(\frac{v_k m T_p}{\lambda} + \frac{BR_k n T_s}{cT_c}\right)} + y_u(n,m) + y_n(n,m) \quad (3)$$

where ρ_k is the signal amplitude of the kth scatterer after dechirping, $n = 1, 2, \ldots, N$ is the sample index in a single chirp, N is the number of samples in a chirp, T_s is the sampling interval at the fast time, $\lambda = c/f_c$ is the wavelength of the chirp signal, $y_u(n,m)$ is the discrete clutter signal, and $y_n(n,m)$ is the discrete white noise.

III. Proposed IL-ULSTI-Based Sleep Posture Recognition Method

As shown in Fig. 1, the proposed IL-ULSTI-based sleep posture recognition method consists of three steps: short-term human state separation, ultra-long-term data sorting and feature extraction, and short-term sleep postures recognition. The core idea is the interactive learning of ultra-long- and short-term information. Specifically, for particular human, we sort and extract personalized features of supine, side, and prone data with the ultra-long-term observation. Also, combined with the personalized ultra-long-term features, the sleep posture recognition is performed with the short-term observation for real-time judgment. From many experiment results, we observe that it is easy to obtain stable information with an ultra-long-term observation. Through interactive learning of ultra-long- and short-term information, we can overcome the differences of scattering characteristics caused by different humans, positions, and ways to stay in bed (e.g., the position of arms and legs, and the way of covering the quilt) and enhance the generalization ability.

A. Short-Term Human State Separation

Three human states, including big movement (such as turning over), lateral posture, and other recumbency, are separated before the fine sleep posture recognition. The separating procedure is mainly conducted by body movement index estimation, big movement detection, RD map calculation, and lateral and nonlateral rough identification.

1) Body Movement Index Estimation: First, we apply the fast Fourier transform (FFT) along the fast time to obtain the range spectrum, denoted as $Y(l,m)$ ($l \in [1, L]$, and L is the range bin index). Then, the incoherent integration [32] is applied to $Y(l,m)$, which can be expressed as

$$S(l,m) = \alpha S(l, m-1) + (1-\alpha) Y(l,m) \quad (4)$$

where $S(l,m)$ represents the signal after incoherent integration and $0 < \alpha < 1$ is the integration factor. Also, the Riemann sum $\mathcal{R}(m)$ of the $|S(l,m)|$ is defined as

$$\mathcal{R}(\bar{m}) = \sum_{l=1}^{L} S(l,m) \quad (5)$$

where $\bar{m} = \lfloor (m/f_r) \rfloor$ represents the $\mathcal{R}(\bar{m})$ is calculated each second. Here, the symbol $\lfloor \cdot \rfloor$ represents the round-down operation, and f_r is the frames per second. Finally, the movement index [33], [34] can be expressed as

$$\mathcal{M}(\bar{m}) = \frac{1}{T_1} \sum_{\tau_1=\bar{m}-T_1+1}^{\bar{m}} \left[\mathcal{R}(\tau_1) - \mathcal{R}(\tau_1)_{\min}\right] \quad (6)$$

where $\mathcal{M}(\bar{m})$ represents the movement index and $\mathcal{R}(\tau_1)_{\min}$ is the minimum value of $\mathcal{R}(\tau_1)$ in the last T_1 seconds.

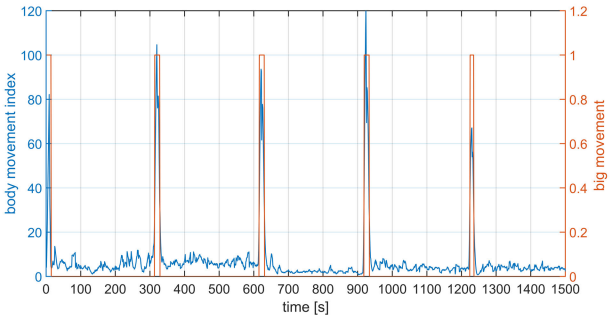

Fig. 2. Results of body movement index estimation and big movement detection.

2) Big Movement Detection: We compare $\mathcal{M}(\bar{m})$ with a threshold $\gamma(\bar{m})$ to check whether the human is moving or not. The big movement detection strategy works as

$$B(\bar{m}) = \begin{cases} 1, & \mathcal{M}(\bar{m}) \geq \gamma(\bar{m}) \\ 0, & \mathcal{M}(\bar{m}) < \gamma(\bar{m}) \end{cases} \tag{7}$$

where $B(\bar{m})$ is the big movement detection result, "1" means the human is drastically moving while "0" is not, and $\gamma(\bar{m})$ is the threshold denoted by

$$\gamma(\bar{m}) = \delta \frac{1}{T_2} \sum_{\tau_2=\bar{m}-T_2+1}^{\bar{m}} \mathcal{M}(\tau_2) \tag{8}$$

where δ is the detection coefficient and T_2 is the duration in seconds.

Fig. 2 shows the results of body movement index estimation and big movement detection. There are four turning over and the human remains in a quiet state for about 5 min among each turning. It can be seen that not only the defined body movement index reasonably describes the intensity of the human movement but also the proposed big movement detection strategy is efficient.

3) RD Map Calculation: In order to eliminate the static environment clutter, we use the background subtraction algorithm [35] described as

$$\widehat{Y}(l,m) = Y(l,m) - \frac{1}{M'} \sum_{i=m-M'+1}^{m} Y(l,m) \tag{9}$$

where M' is the number of frames used for clutter estimation. The FFT along slow time is applied to $\widehat{Y}(l,m)$ to obtain the RD map given by

$$X(l,\omega) = \left| \sum_{k=1}^{K} \widehat{Y}(l,k) w(k) e^{-j\omega k} \right| \tag{10}$$

where $k \in [1, K]$, K is the number of frames used to calculate the Doppler spectrum, $w(k)$ is the Hamming window, and ω is the transform frequency. Then, zero-forcing processing [36] is adopted to the RD map $X(l,\omega)$ to force the values of noises to zeros and keep effective values of micro-Doppler signatures. The cleaner RD map is denoted by $\bar{X}(l,\eta)$, and $\eta \in [1, H]$ is the Doppler frequency index, in which H is the number of FFT points along the slow time.

Fig. 3 shows the RD maps and sketch maps of three recumbent postures, including supine, lateral, and prone postures.

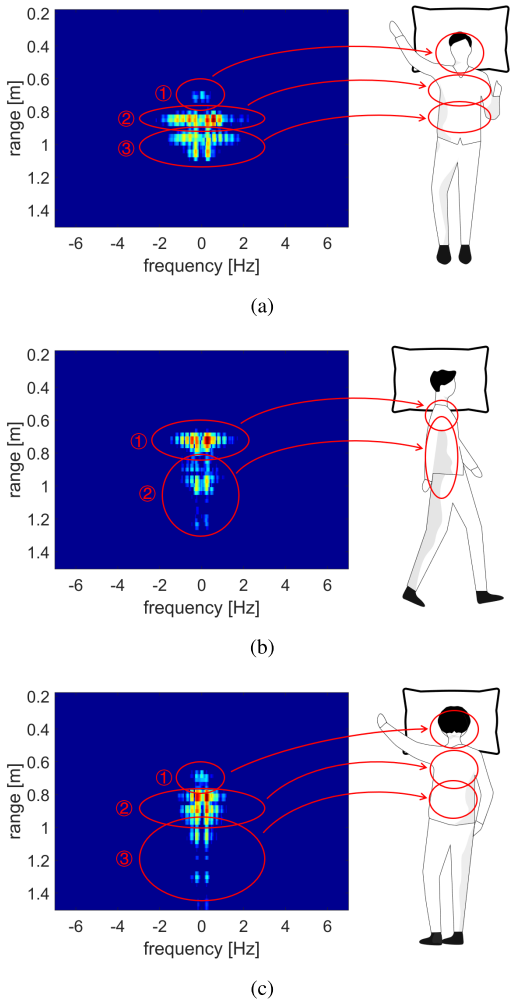

Fig. 3. RD map and sketch map of three recumbent postures. (a) Supine. (b) Lateral. (c) Prone.

When the human is supine, the displacement caused by breathing mainly occurs in the chest and abdomen. In addition, the head of the human is connected to the ribs through the cervical vertebra and thoracic vertebrae. Therefore, the movement of the chest will drive the head and cervical vertebrae to cause a slight displacement. Meanwhile, the face also moves slightly when human breathes through the nasal cavity, which is regarded as a component of the head movement in this work. For a human, the frequency of the displacement is consistent in all parts of the body, but the magnitude is different. As a result, there are differences in the Doppler frequency of various parts of the body. Hence, the scatterers of the human body in the supine posture mainly include the head, the chest, and the abdomen, as shown in Fig. 3(a). The energy and Doppler frequency of the head are much smaller than those of the chest and abdomen. The fluctuation of the side of the chest and abdomen is smaller than that of the front during breathing. Therefore, the energy and Doppler frequency of each scatterer in the lateral recumbency are usually smaller than those in the supine, as shown in Fig. 3(b). Moreover, the movement of the chest drives the movement of the shoulder and arm in the lateral posture. This displacement is close to or even slightly greater than that of the side of the abdomen. Also,

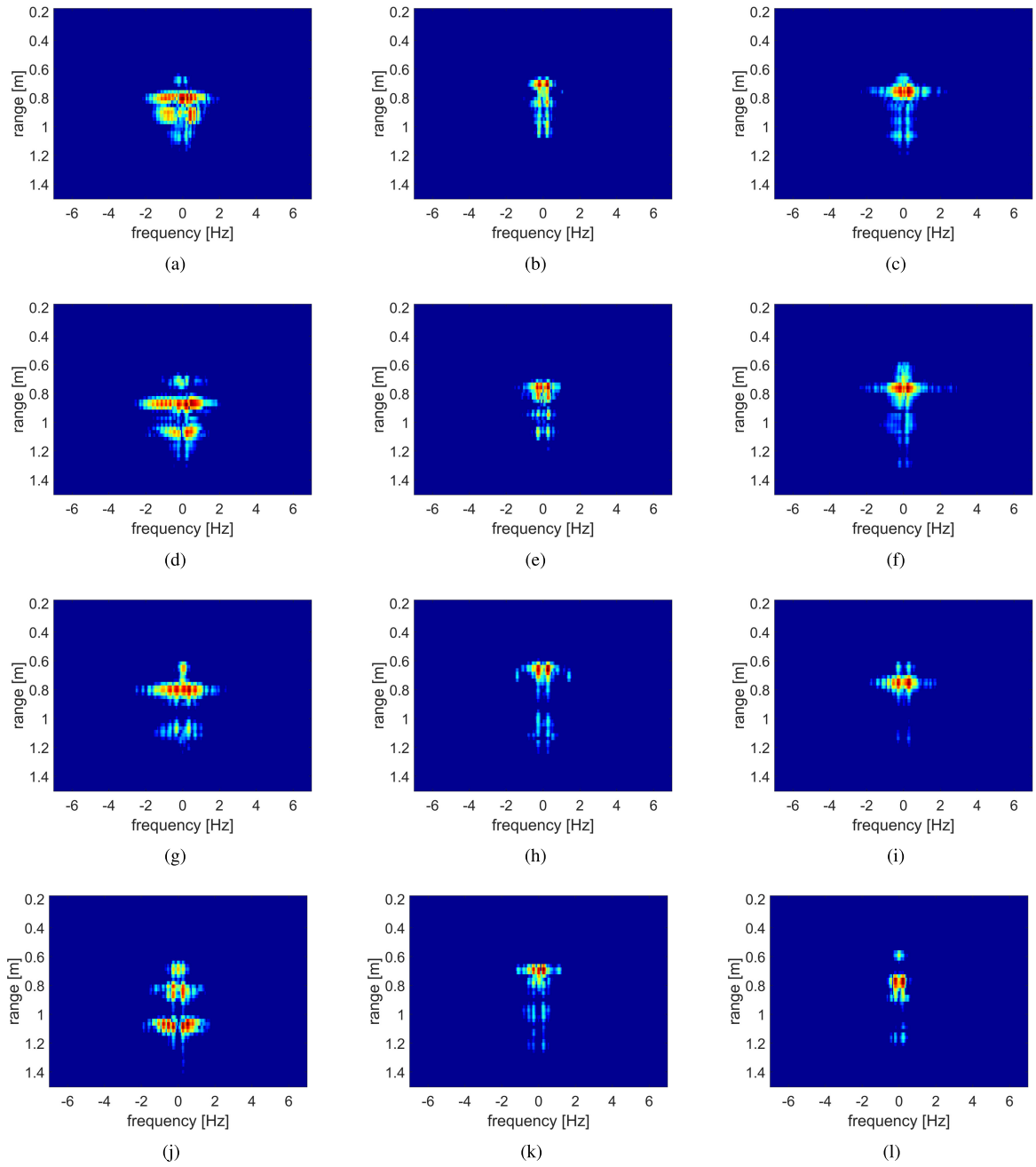

Fig. 4. RD maps of different humans in supine, lateral, and prone posture. (a) Case of supine for human *C*. (b) Case of lateral for human *C*. (c) Case of prone for human *C*. (d) Case of supine for human *F*. (e) Case of lateral for human *F*. (f) Case of prone for human *F*. (g) Case of supine for human *L*. (h) Case of lateral for human *L*. (i) Case of prone for human *L*. (j) Case of supine for human *P*. (k) Case of lateral for human *P*. (l) Case of prone for human *P*.

the scatterers of human in prone posture mainly include the head, the thoracic vertebrae and ribs, and the lumbar vertebrae, as shown in Fig. 3(c). The head is connected with the thoracic vertebrae through the cervical vertebra, and when the thoracic vertebrae move, the movement of the head will be driven. This movement is much smaller than that of the thoracic vertebrae and ribs. In prone posture, the movement of the lumbar vertebrae is usually less than that in the supine because of the compressed abdomen. In addition, the lumbar vertebrae are connected to the thoracic vertebrae, so the movement of the thoracic vertebrae will also drive the movement of the lumbar vertebrae. Also, the movement of the lumbar vertebrae is usually greater than that of the head.

Fig. 4 shows the RD maps for the three sleep postures of six humans, whose information is shown in Table I. The first, second, and third columns in the figure are the RD maps for supine, side, and prone postures, respectively. It is evident that the maps coincide with the above analysis. Furthermore, we can find that there are great differences in the RD map of the same sleep posture of different humans. For example, the energy and Doppler frequency of the chest and abdomen in supine posture vary with the breathing pattern, such as

the human P in the diaphragmatic breathing, as shown in Fig. 4(j). The energy and Doppler frequency of the abdomen are greater than that of the chest. Furthermore, the maximum frequency and the distribution of scatterers of the same sleep posture also vary from person to person. In particular, the maximum frequencies of human F in supine and prone posture are -2.5 and 2.9 Hz, respectively, while that of human P is -1.9 and 0.7 Hz, respectively, as shown in Fig. 4(d), (f), (g), and (i). Also, the energy of the lumbar vertebrae of human C in prone posture is strong, while that of human L is weak, as shown in Fig. 4(c) and (i). Nevertheless, we unexpectedly find that the energy of the nearest for the six humans in lateral posture scatterer is strong, while that in supine and prone is weak. This feature effectively differentiates the lateral posture from the nonlateral posture.

4) Lateral and Nonlateral Rough Identification: Based on the analysis in Section III-A3, it is obvious that the identification of lateral and nonlateral posture is a straightforward item. As a result, we roughly classify the data without big movements into lateral and nonlateral posture. First, the amplitude $[G_1(l)]$ and shape $[G_2(l)$ and $G_3(l)]$ information of the RD map are extracted and expressed as

$$G_1(l) = \sum_{\eta} \bar{X}(l, \eta) \tag{11}$$

$$G_2(l) = \|\boldsymbol{P}_l\|_0 \tag{12}$$

$$G_3(l) = \max_{\eta} Q(l, \eta) - \min_{\eta} Q(l, \eta) \tag{13}$$

where $G_1(l)$ is the amplitude information of RD map along the distance dimension, $G_2(l)$ and $G_3(l)$ are the shape information, the symbol $\|\cdot\|_p$ represents the l_p-norm operation, $\boldsymbol{P}_l = [Q(l, 1), Q(l, 2), \ldots, Q(l, H)]^{\mathrm{T}}$, and $Q(l, \eta)$ is denoted as

$$Q(l, \eta) = \begin{cases} \eta, & \bar{X}(l, \eta) > 0 \\ 0, & \bar{X}(l, \eta) = 0. \end{cases} \tag{14}$$

Then, the amplitude characteristics of salient points of different parts of human are extracted from $G_1(l)$, denoted as

$$F_1 = \frac{G_1(L_2)}{\max\ G_1(l)} \tag{15}$$

$$F_2 = \frac{G_1(L_3)}{\max\ G_1(l)} \tag{16}$$

$$F_3 = \frac{G_{1_{2\mathrm{nd}}}}{\max\ G_1(l)} \tag{17}$$

$$F_4 = \frac{G_{1_{3\mathrm{rd}}}}{\max\ G_1(l)} \tag{18}$$

where L_2 and L_3 are the indices of the second and third range bins occupied by the human, respectively, and $G_{1_{2\mathrm{nd}}}$ and $G_{1_{3\mathrm{rd}}}$ represent the amplitude of the second and third peaks of $G_1(l)$, respectively.

Also, the head size features F_5 and F_6 are extracted from $G_2(l)$ and $G_3(l)$, respectively, expressed as

$$F_5 = \left\|\bar{\boldsymbol{\Gamma}}\right\|_0 \tag{19}$$

where $\bar{\boldsymbol{\Gamma}} = [\Gamma(1), \Gamma(2), \ldots, \Gamma(L)]$ is a vector. Here, $\Gamma(l)$ is denoted as

$$\Gamma(l) = \begin{cases} 1, & 0 < G_2(l) < \varepsilon G_{2m} \wedge l < l' \\ 0, & \text{other} \end{cases} \tag{20}$$

where ε is the threshold, G_{2m} is the maximum value of $G_2(l)$, and l' is the index corresponding to G_{2m}. Also, F_6 is given by

$$F_6 = \left\|\bar{\boldsymbol{\Theta}}\right\|_0 \tag{21}$$

where $\bar{\boldsymbol{\Theta}} = [\Theta(1), \Theta(2), \ldots, \Theta(L)]$ is a vector. Here, $\Theta(l)$ is denoted as

$$\Theta(l) = \begin{cases} 1, & 0 < G_3(l) < \varepsilon G_{3m} \wedge l < l'' \\ 0, & \text{other} \end{cases} \tag{22}$$

where G_{3m} is the maximum value of $G_3(l)$ and l'' is the index corresponding to G_{3m}.

Finally, an AdaBoost classifier is applied to identify the lateral and nonlateral posture. The input features are the amplitude and shape features of RD map, namely, $\boldsymbol{F} = [F_1, F_2, \ldots, F_6]^{\mathrm{T}}$. Also, the output is $\mathcal{Z}$. The AdaBoost classifier consists of 30 DTs, which are linearly combined to construct an accurate classifier.

B. Ultra-Long-Term Data Sorting and Feature Extraction

The ultra-long-term data can be divided into multiple segments without motions based on the occurrences of big movements. Moreover, we assume that the human maintains the same posture in a segment. In this section, we will sort the data of supine, lateral, and supine postures for a specific human over a long period of time (e.g., several to tens of minutes). Then, we extract the personalized ultra-long-term features for this human. The whole procedure can be divided into three parts.

1) Data Sorting of Lateral and Nonlateral: First, a voting strategy is applied to sort the lateral and nonlateral posture based on the rough identification output $\mathcal{Z}$ in a segment. In short, it is to follow the principle that the minority is subordinate to the majority. When more than half of the outputs of a segment are lateral, this segment is sorted as lateral, otherwise as nonlateral. The number of outputs used for voting depends on the length of the segment.

2) Data Sorting of Supine and Prone: Here, two features are proposed to sort supine and prone data. The first is the maximum Doppler frequency of the torsos, computed by

$$F_7 = \max\left(|f_{+\max}|, |f_{-\max}|\right) \tag{23}$$

where $f_{+\max}$ and $f_{-\max}$ represent the maximum Doppler frequency in the positive and negative frequency ranges of $\bar{X}(l, \eta)$, respectively. The second is the distribution characteristic of human micromotion frequency, given by

$$F_8 = \|\boldsymbol{C_1}\|_0 \tag{24}$$

where $\boldsymbol{C_1}$ represent the vector $[W(1), W(2), \ldots, W(H)]^{\mathrm{T}}$. Here, $W(\eta)$ is denoted as

$$W(\eta) = \begin{cases} 1, & G_4(\eta) \geq \zeta_1 \max\ G_4(\eta) \\ 0, & \text{other} \end{cases} \tag{25}$$

where $G_4(\eta) = \sum_l \bar{X}(l, \eta)$ and ζ_1 is a threshold.

For I segments sorted as nonlateral, the ratios of the features F_7 and F_8 of each two segments are calculated by

$$\mathbf{\Lambda}^1 = \begin{bmatrix} \mu^1_{1,1} & \cdots & \mu^1_{1,I} \\ \vdots & \ddots & \vdots \\ \mu^1_{I,1} & \cdots & \mu^1_{I,I} \end{bmatrix} \tag{26}$$

$$\mathbf{\Lambda}^2 = \begin{bmatrix} \mu^2_{1,1} & \cdots & \mu^2_{1,I} \\ \vdots & \ddots & \vdots \\ \mu^2_{I,1} & \cdots & \mu^2_{I,I} \end{bmatrix} \tag{27}$$

where $\mathbf{\Lambda}^1$ and $\mathbf{\Lambda}^2$ are the ratios of features F_7 and F_8, respectively, and $i, j \in [1, I]$ is the index of the segments. $\mu^1_{i,j} = \text{NaN}$, $\mu^2_{i,j} = \text{NaN}$ when $i = j$; otherwise, they can be expressed as

$$\mu^1_{i,j,i\neq j} = \begin{cases} \text{supine} \rightarrow \text{prone}, & 0 < r^1_{i,j} < \beta^1_{\text{lower}} \\ \text{NaN}, & \beta^1_{\text{lower}} \leq r^1_{i,j} \leq \beta^1_{\text{upper}} \\ \text{prone} \rightarrow \text{supine}, & r^1_{i,j} > \beta^1_{\text{upper}} \end{cases} \tag{28}$$

$$\mu^2_{i,j,i\neq j} = \begin{cases} \text{supine} \rightarrow \text{prone}, & 0 < r^2_{i,j} < \beta^2_{\text{lower}} \\ \text{NaN}, & \beta^2_{\text{lower}} \leq r^2_{i,j} \leq \beta^2_{\text{upper}} \\ \text{prone} \rightarrow \text{supine}, & r^2_{i,j} > \beta^2_{\text{upper}} \end{cases} \tag{29}$$

where NaN represents the inability to make a judgment, $r^1_{i,j}$ is the ratio of F_7 of the ith segment to the jth segment, $r^2_{i,j}$ is the ratio of F_8 of the ith segment to the jth segment, and β^1_{lower}, β^1_{upper}, β^2_{lower} and β^2_{upper} are the thresholds. If both $\mathbf{\Lambda}^1$ and $\mathbf{\Lambda}^2$ are NaN, adjust the decision thresholds β^1_{lower}, β^1_{upper}, β^2_{lower}, and β^2_{upper} and then recalculate $\mathbf{\Lambda}^1$ and $\mathbf{\Lambda}^2$. Finally, $\mathbf{\Lambda}^1$ and $\mathbf{\Lambda}^2$ are combined to vote on each segment to select the supine and prone data segments.

3) Personalized Features Extraction: Through the ultra-long-term data sorting, we can select the supine and prone segments. Thus, the effective features $\tilde{\boldsymbol{F}} = [F_7, F_8, \ldots, F_{11}]^{\text{T}}$ of supine and prone posture, i.e., personalized ultra-long-term features, can be extracted and denoted as $\boldsymbol{F}_{\text{supine}}$ and $\boldsymbol{F}_{\text{prone}}$, respectively. Another distribution characteristic of human micromotion frequency is described by

$$F_9 = \|\boldsymbol{C_2}\|_0 \tag{30}$$

where $\boldsymbol{C_2}$ represent the vector $[W(1), W(2), \ldots, W(H)]^{\text{T}}$ with the threshold ζ_2 (a higher value than ζ_1). Also, the last two features are the amplitude distribution characteristics of human scatterers, given by

$$F_{10} = \frac{1}{l_1} \sum_{l=L_0}^{L_0+l_1-1} \left[G_1(l) - \frac{1}{l_1} \sum_{l=L_0}^{L_0+l_1-1} G_1(l) \right]^2 \tag{31}$$

$$F_{11} = \frac{1}{l_2} \sum_{l=L_0}^{L_0+l_2-1} \left[G_1(l) - \frac{1}{l_2} \sum_{l=L_0}^{L_0+l_2-1} G_1(l) \right]^2 \tag{32}$$

where L_0 is the index of the nearest distance from the human to the radar and l_1 and l_2 represent the number of range bins.

TABLE I
PHYSICAL INFORMATION OF PARTICIPANTS

Participant	A	B	C	D	E	F	G	H
Gender(F/M)	F	F	F	F	F	F	F	M
Height(cm)	150	153	158	158	159	163	168	180
Weight(kg)	48	47	41	44	46	51	60	80
Participant	I	J	K	L	M	N	O	P
Gender(F/M)	M	M	M	M	M	M	M	M
Height(cm)	160	167	167	169	170	170	174	178
Weight(kg)	46	58	57	60	57	59	67	65

C. Short-Term Sleep Postures Recognition

1) Lateral and Nonlateral Classification: For short-term (e.g., a few seconds or minutes) data, similarly, we apply the voting strategy to classify the lateral and nonlateral posture based on the rough identification output $\mathcal{Z}$. It is worth noting that here, we only use the outputs within 15 s after the big movement to vote. If more than half of the outputs within 15 s are lateral, the current sleep posture is lateral, and otherwise, further detection will be performed.

2) Supine and Prone Detection: The detection based on personalized ultra-long-term features is employed to further classify supine and prone posture if the current sleep posture is nonlateral posture.

When the current posture is the first one or the previous one is nonlateral posture, we make judgments based on the nearest neighbor principle. Specifically, the distance d_{su} between the current sleep posture feature vector $\boldsymbol{F}_{\text{now}}$ and $\boldsymbol{F}_{\text{supine}}$, and the distance d_{pr} between $\boldsymbol{F}_{\text{now}}$ and $\boldsymbol{F}_{\text{prone}}$ are, respectively, calculated by

$$d_{\text{su}} = \sqrt{\sum_{\varphi=1}^{\Phi} \left(F_{\text{now},\varphi} - F_{\text{supine},\varphi} \right)^2} \tag{33}$$

$$d_{\text{pr}} = \sqrt{\sum_{\varphi=1}^{\Phi} \left(F_{\text{now},\varphi} - F_{\text{prone},\varphi} \right)^2} \tag{34}$$

where Φ is the number of the features used for short-term sleep posture recognition and $F_{\text{now},\varphi}$, $F_{\text{supine},\varphi}$, and $F_{\text{prone},\varphi}$ are the φth feature in $\boldsymbol{F}_{\text{now}}$, $\boldsymbol{F}_{\text{supine}}$, and $\boldsymbol{F}_{\text{prone}}$, respectively. If $d_{\text{su}} < d_{\text{pr}}$, the current sleep posture is supine, and otherwise, it is prone.

We calculate the ratio $r_{\text{now}}(\varphi)$ of $\boldsymbol{F}_{\text{now}}$ to the previous sleep posture feature vector $\boldsymbol{F}_{\text{pre}}$, which is denoted as

$$r_{\text{now}}(\varphi) = \begin{cases} 1, & \dfrac{F_{\text{now},\varphi}}{F_{\text{pre},\varphi}} > 1 \\ 0, & \text{other} \end{cases} \tag{35}$$

where $F_{\text{pre},\varphi}$ is the φth feature in $\boldsymbol{F}_{\text{pre}}$. If $\sum_{\varphi=1}^{\Phi} r_{\text{now}}(\varphi) > (\Phi/2)$, the current sleep posture is supine, and otherwise, it is prone.

IV. EXPERIMENT AND RESULTS

The front and back of the designed radar sensing module are shown in Fig. 5(a) and (b), respectively. It integrates antennas, radio, and digital baseband, and transmits, receives, and digit

TABLE II
CONFUSION MATRICES OF ULTRA-LONG-TERM LATERAL AND NONLATERAL SORTING

TTS				LOOCV			
Accuracy (%)		Predicted class		Accuracy (%)		Predicted class	
		lateral	non-lateral			lateral	non-lateral
Actual class	lateral	**91.0**	9.0	Actual class	lateral	**90.5**	9.5
	non-lateral	2.1	**97.9**		non-lateral	6.9	**93.1**

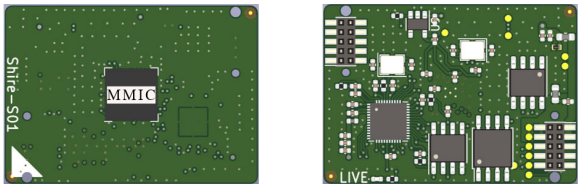

(a) (b)

Fig. 5. Radar sensing module. (a) Front. (b) Back.

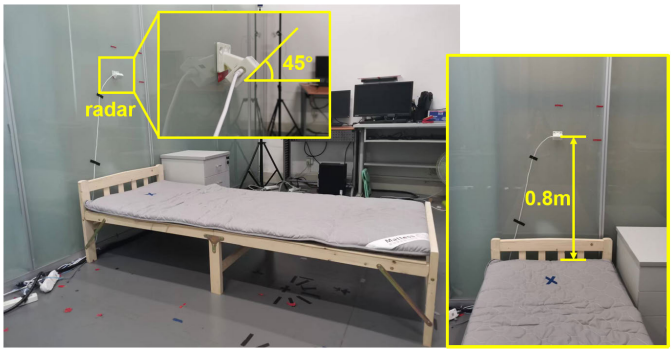

Fig. 6. Experimental bedroom-like environment.

TABLE III
CONFUSION MATRIX OF ULTRA-LONG-TERM DATA SORTING

Accuracy (%)		Predicted class			
		supine	lateral	prone	other
Actual class	supine	**77.6**	0.6	4.0	17.8
	lateral	0	**89.5**	5.3	5.3
	prone	7.0	1.3	**70.7**	21.0
	other	0	0	0	**0**

samples the signal. The millimeter-wave integrated circuit (MMIC) used is the SC1221AR3 produced by Socionext Company with a length and width of 9 mm.

As shown in Fig. 6, the radar was installed on the wall with 0.8 m height above the bed, and the main lobe of the radar antenna is 45° downward toward the bed. There are 16 volunteers in the experiment, including nine males and seven females. Table I shows the physical information and of all participants. In the experiment, participants were instructed to lie within the detection range of the radar and perform seven movements: SULA, SUPR, LASU, lateral to another lateral (LALA), lateral to prone (LAPR), PRSU, and prone to lateral (PRLA). Lying on the left side and the right side is not distinguished, collectively referred to as lateral posture. The participants were given 3 min to lie peacefully with steady breathing before performing the next action to obtain stable characteristics of the sleep posture. A total of 660 samples from all participants were recorded, including 209 supine postures, 262 lateral postures, and 189 prone postures.

A. Results of Ultra-Long-Term Data Sorting

Here, we first randomly divide the labeled data into the training set and testing set by train–test splitting (TTS) to verify the lateral and nonlateral data sorting strategy. In addition, in order to verify the robustness of the lateral and nonlateral data sorting strategy for different humans, we use the leave-one-out cross validation (LOOCV) to divide the data. Specifically, the data of a certain participant are selected for testing, and the rest of the data are used to train the classifier. The confusion matrices of TTS and LOOCV are shown in Table II. It can be seen that the overall accuracy of TTS is 95.2%, the average true positive rate is 91%, and the average false positive rate is 2.1%. Also, the overall accuracy of LOOCV is 92.1%, the average true positive rate is 90.5%, and the average false positive rate is 6.9%. Although the accuracy of LOOCV is lower than that of TTS, the overall accuracy of the former can exceed 92%. This verifies that the proposed ultra-long-term data sorting strategy for lateral and nonlateral is robust to different humans.

Second, in order to illustrate the feasibility of the proposed ultra-long-term data sorting strategy for supine and prone, we analyze the distribution of five features F_7–F_{11} for supine and prone, as shown in Fig. 7. The first row in Fig. 7 is the box plot of F_7–F_{11} of all participants, the second row is for participant G, and the third row is for participant P. It can be seen that for all participants, there are large overlaps in the distributions of supine and prone of the five features. Therefore, it is difficult to use these features to classify supine and prone data by a single classifier that can be adapted to different humans. Also, for a specific participant, such as participant G, the distribution of the five characteristics of supine and prone is essentially not overlapping. For participant P, although the overlap degree of F_{11} is relatively large, those between the two sleep postures of the other four features are relatively small or even zero. This proves that these five features are much suitable for classification of supine and prone postures for a specific participant. Therefore, we can sort supine and prone data separately for each participant. Furthermore, we can apply the personalized learning to realize sleep posture recognition, which can adapt to different humans. Specifically, we count the ratios distribution of feature F_7 and F_8, as shown in Fig. 8. Among them, Fig. 8(a) shows the histogram of the ratios of SUPR and PRSU for F_7, and the magenta dotted line and blue dotted line represent the selection of parameter β^1_{lower} and β^1_{upper}, respectively. Also, Fig. 8(b) shows the histogram of the ratios of SUPR and PRSU for

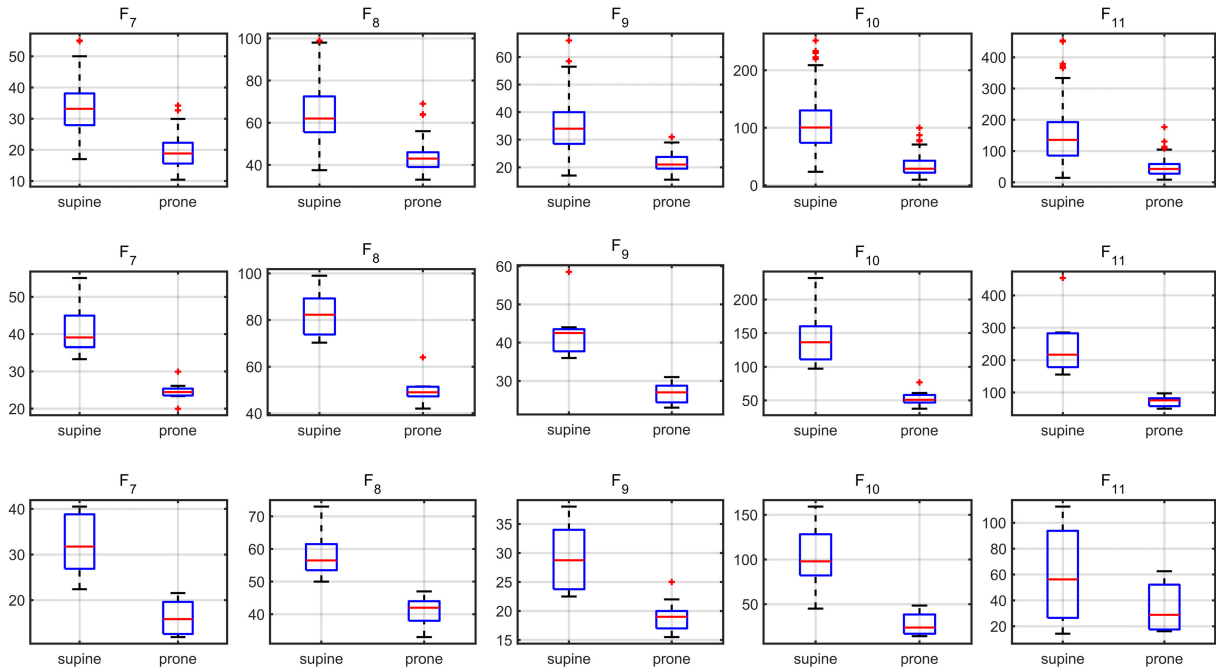

Fig. 7. Distribution box plots of supine and prone in different situations.

TABLE IV
CONFUSION MATRICES OF LATERAL AND NONLATERAL CLASSIFICATION

TTS				LOOCV			
Accuracy (%)		Predicted class		Accuracy (%)		Predicted class	
		lateral	non-lateral			lateral	non-lateral
Actual class	lateral	**88.7**	11.3	Actual class	lateral	**89.1**	10.9
	non-lateral	2.1	**97.9**		non-lateral	5.2	**94.8**

F_8, and the magenta dotted line and blue dotted line represent the selection of parameter β^2_{lower} and β^2_{upper}, respectively. It is obvious that, for both F_7 and F_8, there are slight overlaps between the ratio distributions of the SUPR and PRSU. As a result, it is feasible to sort data of supine and prone with an ultra-long-term observation according to the ratios of the features between two segments in Section III-B2. According to the statistical results, it can be seen that the smaller β^1_{lower} and β^2_{lower}, the greater the miss rate for SUPR. The larger β^1_{upper} and β^2_{upper}, the greater the miss rate for PRSU. Also, the greater the gaps between β^1_{lower} and β^1_{upper}, and β^2_{lower} and β^2_{upper}, the more results unable to make a judgment.

Third, Table III shows the results of ultra-long-term data sorting, where "other" is an indeterminate category other than supine, lateral, and prone. It is obvious that some of the three sleep postures are sorted as "other," with an overall accuracy of 80.2%. However, the data classified as other will be discarded and not used for personalized ultra-long-term feature extraction and sleep posture recognition subsequently. When the other category is not considered, the overall accuracy of the sorting can reach 93.1%, which shows the effectiveness of the proposed ultra-long-term data sorting strategy.

B. Results of Short-Term Sleep Postures Recognition

In the fourth example, the TTS and LOOCV strategies are used to demonstrate the validity of the short-term lateral and nonlateral classification strategy, and Table IV shows the confusion matrices. It can be seen that the overall accuracy of TTS is 94.3%, the average true positive rate is 88.7%, and the average false positive rate is 2.1%. Also, the overall LOOCV is 92.6%, the average true positive rate is 89.1%, and the average false positive rate is 5.2%. The accuracy of LOOCV is close to that of TTS, indicating that there is strong robustness of this strategy for different humans. It is worth noting that the accuracy of short-term lateral and nonlateral classification is slightly lower than that of ultra-long term, which is due to more data used for decision of the latter.

TABLE V
CONFUSION MATRIX OF SLEEP POSTURE RECOGNITION

Accuracy (%)		Predicted class		
		supine	lateral	prone
Actual class	supine	**92.8**	0	7.2
	lateral	0.6	**91.2**	8.2
	prone	6.3	4.8	**88.9**

Tables V and VI show the recognition results of considering the sleep posture and the SPC, respectively. When simply focusing on sleep posture recognition, the proposed IL-ULSTI-based sleep posture recognition method has a high positive rate for supine and lateral, but it is easy to misjudge prone posture as supine or lateral, and the overall accuracy can reach

TABLE VI
CONFUSION MATRIX OF SPC RECOGNITION

Accuracy (%)		Predicted class							
		SULA	SUPR	LASU	LALA	LAPR	PRSU	PRLA	other
Actual class	SULA	**81.7**	6.7	0	0	0	0	11.7	0
	SUPR	5.9	**85.3**	0	0	0	0	11.7	8.8
	LASU	0	0	**89.6**	0	4.2	6.3	0	0
	LALA	0	0	0	**84.0**	10.0	0	6.0	0
	LAPR	0	1.8	3.6	3.6	**78.6**	5.4	0	7.1
	PRSU	0	0	4.2	0	0	**89.6**	0	6.3
	PRLA	10.9	2.2	0	2.2	0	2.2	**76.1**	6.5
	other	0	0	0	0	0	0	0	**100**

TABLE VII
COMPARISON WITH OTHER WORKS

works	Participants	Num. of postures	Technologies, installation method	Num. of sensors	Method	Num. of samples	Consider SPC	Result
Kiriazi et al. [20]	20	3	CW radar OTC	2	Detection	60	✕	2.4GHz: 90% 5.8GHz: 80% Dual: 100%
Islam et al. [22]	20	3	CW radar OTC	2	DT, KNN, SVM	300	✕	2.4GHz: 85% 5.8GHz: 80% Dual: 98.4%
Lai et al. [26]	18	4	UWB radar OTC & STB	2	LR, RF, XGBoost, SVM	720	✕	Top: 75% Side: 75% Dual: 93.8%
Piriyajitakonkij et al. [31]	38	5[1]	UWB radar, ATB	1	DCNN, MVL	1436	✓	73.7%
Our work	**17**	**8[2]**	**FMCW radar, ATB**	**1**	**IL-ULSTI**	**660**	✓	**SP: 91% SPC: 83.7%**

OTC: on the ceiling; STB: on the side of the bed; ATB: above the bed.
LR: logistic regression; RF: random forest.
SP: Sleep Posture.
[1] Here, there are five categories including SULA, SUPR, LASU, PRSU, and other.
[2] Here, there are eight categories including SULA, SUPR, LASU, LALA, LAPR, PRSU, PRLA, and other.

91%. Considering SPC, the overall accuracy of the proposed IL-ULSTI-based sleep posture recognition method can reach 83.68%, in which LASU and PRSU have the highest true positive rate, while PRLA has the lowest true positive rate and is easy to be misjudged as SULA.

C. Comparison With Other State-of-the-Art Methods

In the last example, we compare the performance of our work with other state-of-the-art sleep posture recognition methods in Table VII. Among these works, works [20], [22], and [26] merely classified various sleep postures, while our work and work [31] have considered the conversion of sleep posture. In [20], the effective RCS and torso displacement of the supine, lateral, and prone postures were analyzed and studied in depth, and the sleep posture was accurately recognized through the dual-frequency decision algorithm with supine taken as a reference. In the follow-up work, this team tried to use an optimizable TML classifiers to recognize sleep postures, and the accuracy of 2.4 GHz, 5.8 GHz, and dual-frequency measurements is 85%, 80%, and 98.4%, respectively [22]. It is worth noting that work [31] considered the conversion of sleep postures, including SULA, SUPR, LASU, PRSU, and other, with the recognition accuracy of 73.7%, while the proposed IL-ULSTI-based sleep posture recognition method recognizes three sleep postures with an accuracy of 91% and 83.7% when considering SPC by using a single radar.

Recording the computational complexity, we note that the total number of multiplications for the method in [31] is $N_c \times N_l \times 9332 + N_l \times N_l \times 860 + 440$, the additions is $N_c \times N_l \times 7780 + N_l \times N_l \times 650 + 426$, and the required parameters is $N_c \times N_l \times 66 + N_l \times N_l \times 84 + 10\,220$. Here, $N_c = 40$, $N_l = 160$, and $N_c \times N_l$ and $N_l \times N_l$ are the sizes of the input maps, while for our proposed IL-ULSTI-based sleep posture recognition method, the AdaBoost classifier only requires 30 multiplications, 179 additions, and 3030 parameters, which is much lower than that of the DNN methods. Here, from this point of view, our proposed IL-ULSTI-based sleep posture recognition method exhibits a relatively low

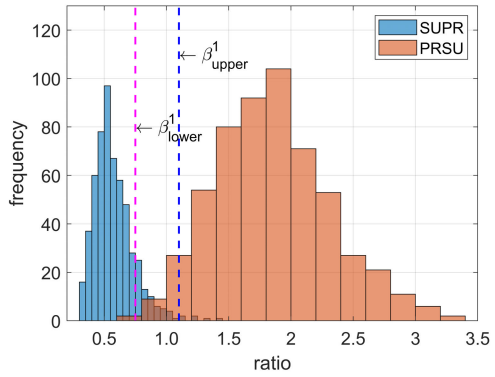

(a)

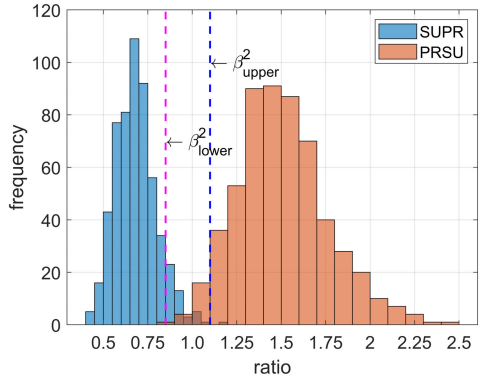

(b)

Fig. 8. Histogram of ratios between two segments. (a) Case of F_7. (b) Case of F_8.

complexity and is suitable for the edge appliance with low consumption.

V. Conclusion

In this article, we propose a human sleep posture recognition method based on IL-ULSTI. First, we analyzed the RD maps of different sleep postures and found that the distribution and intensity of body scatterers vary by sleeping posture. As a result, in order to improve the generalization ability of different people, we applied interactive learning on sleep posture recognition. Specifically, we first sorted and extracted the personalized features with an ultra-long-term observation. Subsequently, combined with the extracted personalized ultra-long-term features, we achieved recognition of sleep posture and SPC with a short-term observation for real-time judgment. Finally, we conducted sufficient experiments to analyze the performance of the proposed IL-ULSTI-based sleep posture recognition method. Also, the results have shown that the recognition accuracy of the proposed IL-ULSTI-based sleep posture recognition method for the three sleep postures of supine, lateral, and prone can reach 91% and 83.7% for eight SPC categories, including SULA, SUPR, LASU, LALA, LAPR, PRSU, PRLA, and other. Compared with other state-of-the-art methods, we not only took into account the conversion of sleep posture but also realized the sleep posture recognition adapting to different humans through interactive learning in a low-complexity manner.

References

[1] A. Menon and M. Kumar, "Influence of body position on severity of obstructive sleep apnea: A systematic review," *Int. Scholarly Res. Notices*, vol. 2013, no. 670381, pp. 1–7, Otc. 2013.

[2] A. Oksenberg, I. Khamaysi, D. S. Silverberg, and A. Tarasiuk, "Association of body position with severity of apneic events in patients with severe nonpositional obstructive sleep apnea," *Chest*, vol. 118, no. 4, pp. 1018–1024, Oct. 2000.

[3] S. Isono, A. Shimada, M. Utsugi, A. Konno, and T. Nishino, "Comparison of static mechanical properties of the passive pharynx between normal children and children with sleep-disordered breathing," *Amer. J. Respiratory Crit. Care Med.*, vol. 157, no. 4, pp. 1204–1212, Apr. 1998.

[4] N. Goldberg, Y. Rodriguez-Prado, R. Tillery, and C. Chua, "Comparison of static mechanical properties of the passive pharynx between normal children and children with sleep-disordered breathing," *Pediatric Ann.*, vol. 47, no. 3, pp. e118–e123, 2018.

[5] K.-M. Chang and S.-H. Liu, "Wireless portable electrocardiogram and a tri-axis accelerometer implementation and application on sleep activity monitoring," *Telemedicine e-Health*, vol. 17, no. 3, pp. 177–184, Apr. 2011.

[6] H. Yoon et al., "Estimation of sleep posture using a patch-type accelerometer based device," in *Proc. 37th Annu. Int. Conf. IEEE Eng. Med. Biol. Soc. (EMBC)*, Milan, Italy, Aug. 2015, pp. 4942–4945.

[7] M. Borazio and K. Van Laerhoven, "Combining wearable and environmental sensing into an unobtrusive tool for long-term sleep studies," in *Proc. 2nd ACM SIGHIT Int. Health Informat. Symp.*, New York, NY, USA, Jan. 2012, pp. 71–80.

[8] J. Ahn, S. Lee, S. Kang, H. Han, and B. M. Lee, "In-sleep activity detecting algorithm for sleepcare system," in *Proc. IEEE 14th Int. Conf. Semantic Comput. (ICSC)*, San Diego, CA, USA, Feb. 2020, pp. 350–353.

[9] A. Channa, M. Yousuf, and N. Popescu, "Machine learning algorithms for posture identification of obstructive sleep apnea patients using IoT solutions," in *Proc. Int. Conf. e-Health Bioeng. (EHB)*, Iasi, Romania, Oct. 2020, pp. 1–6.

[10] S. M. Mohammadi, M. Alnowami, S. Khan, D.-J. Dijk, A. Hilton, and K. Wells, "Sleep posture classification using a convolutional neural network," in *Proc. 40th Annu. Int. Conf. IEEE Eng. Med. Biol. Soc. (EMBC)*, Honolulu, HI, USA, Jul. 2018, pp. 1–6.

[11] Y.-Y. Li, S.-J. Wang, and Y.-P. Hung, "A vision-based system for in-sleep upper-body and head pose classification," *Sensors*, vol. 22, no. 5, p. 2014, Mar. 2022.

[12] S. Milici, J. Lorenzo, A. Lázaro, R. Villarino, and D. Girbau, "Wireless breathing sensor based on wearable modulated frequency selective surface," *IEEE Sensors J.*, vol. 17, no. 5, pp. 1285–1292, Mar. 2017.

[13] T. Grimm, M. Martinez, A. Benz, and R. Stiefelhagen, "Sleep position classification from a depth camera using bed aligned maps," in *Proc. 23rd Int. Conf. Pattern Recognit. (ICPR)*, Cancun, Mexico, Dec. 2016, pp. 319–324.

[14] S. Akbarian, G. Delfi, K. Zhu, A. Yadollahi, and B. Taati, "Automated non-contact detection of head and body positions during sleep," *IEEE Access*, vol. 7, pp. 72826–72834, 2019.

[15] Z. Yang, P. H. Pathak, Y. Zeng, X. Liran, and P. Mohapatra, "Vital sign and sleep monitoring using millimeter wave," *ACM Trans. Sensor Netw.*, vol. 13, no. 2, pp. 1–32, May 2017.

[16] X. Liu, J. Cao, S. Tang, and J. Wen, "Wi-sleep: Contactless sleep monitoring via WiFi signals," in *Proc. IEEE Real-Time Syst. Symp.*, Rome, Italy, Dec. 2014, pp. 346–355.

[17] J. Liu, Y. Chen, Y. Wang, X. Chen, J. Cheng, and J. Yang, "Monitoring vital signs and postures during sleep using WiFi signals," *IEEE Internet Things J.*, vol. 5, no. 3, pp. 2071–2084, Jun. 2018.

[18] Y. Cao et al., "Contactless body movement recognition during sleep via WiFi signals," *IEEE Internet Things J.*, vol. 7, no. 3, pp. 2028–2037, Mar. 2020.

[19] J. E. Kiriazi, O. Boric-Lubecke, and V. M. Lubecke, "Dual-frequency technique for assessment of cardiopulmonary effective RCS and displacement," *IEEE Sensors J.*, vol. 12, no. 3, pp. 574–582, Mar. 2012.

[20] J. E. Kiriazi, S. M. M. Islam, O. Boric-Lubecke, and V. M. Lubecke, "Sleep posture recognition with a dual-frequency cardiopulmonary Doppler radar," *IEEE Access*, vol. 9, pp. 36181–36194, 2021.

[21] P. Nguyen, X. Zhang, A. Halbower, and T. Vu, "Continuous and fine-grained breathing volume monitoring from afar using wireless signals," in *Proc. 35th Annu. IEEE Int. Conf. Comput. Commun. (INFOCOM)*, San Francisco, CA, USA, Apr. 2016, pp. 1–9.

[22] S. M. M. Islam and V. M. Lubecke, "Sleep posture recognition with a dual-frequency microwave Doppler radar and machine learning classifiers," *IEEE Sensors Lett.*, vol. 6, no. 3, pp. 1–4, Mar. 2022.

[23] P. Nguyen, X. Zhang, A. C. Halbower, and T. Vu, "Poster: Continuous and fine-grained respiration volume monitoring using continuous wave radar," in *Proc. 21st Annu. Int. Conf. Mobile Comput. Netw.*, New York, NY, USA, Sep. 2015, pp. 266–268.

[24] K. Higashi, G. Sun, and K. Ishibashi, "Precise heart rate measurement using non-contact Doppler radar assisted by machine-learning-based sleep posture estimation," in *Proc. 41st Annu. Int. Conf. IEEE Eng. Med. Biol. Soc. (EMBC)*, Berlin, Germany, Jul. 2019, pp. 788–791.

[25] S. Vishwakarma and S. S. Ram, "Mitigation of through-wall distortions of frontal radar images using denoising autoencoders," *IEEE Trans. Geosci. Remote Sens.*, vol. 58, no. 9, pp. 6650–6663, Sep. 2020.

[26] D. K.-H. Lai et al., "Dual ultra-wideband (UWB) radar-based sleep posture recognition system: Towards ubiquitous sleep monitoring," *Engineered Regener.*, vol. 4, no. 1, pp. 36–43, Mar. 2023.

[27] X. Li, Y. He, and X. Jing, "A survey of deep learning-based human activity recognition in radar," *Remote Sens.*, vol. 11, no. 9, p. 1068, May 2019.

[28] Z. Zheng, D. Zhang, X. Liang, X. Liu, and G. Fang, "Unsupervised human contour extraction from through-wall radar images using dual UNet," *IEEE Geosci. Remote Sens. Lett.*, vol. 20, pp. 1–5, 2023.

[29] S. Yue, Y. Yang, H. Wang, H. Rahul, and D. Katabi, "BodyCompass: Monitoring sleep posture with wireless signals," *Proc. ACM Interact., Mobile, Wearable Ubiquitous Technol.*, vol. 4, no. 2, pp. 1–25, Jun. 2020.

[30] Z. Zheng et al., "Recovering human pose and shape from through-the-wall radar images," *IEEE Trans. Geosci. Remote Sens.*, vol. 60, 2022, Art. no. 5112015.

[31] M. Piriyajitakonkij et al., "SleepPoseNet: Multi-view learning for sleep postural transition recognition using UWB," *IEEE J. Biomed. Health Informat.*, vol. 25, no. 4, pp. 1305–1314, Apr. 2021.

[32] Z. Yang, G. Qi, and R. Bao, "Indoor regional people counting method based on bi-motion-model-framework using UWB radar," *IEEE Geosci. Remote Sens. Lett.*, vol. 19, pp. 1–5, 2022.

[33] J. M. Lee, J. W. Choi, and S. H. Cho, "Movement analysis during sleep using an IR-UWB radar sensor," in *Proc. IEEE Int. Conf. Netw. Infrastruct. Digit. Content (IC-NIDC)*, Beijing, China, Sep. 2016, pp. 486–490.

[34] M. Kagawa, N. Sasaki, K. Suzumura, and T. Matsui, "Sleep stage classification by body movement index and respiratory interval indices using multiple radar sensors," in *Proc. 37th Annu. Int. Conf. IEEE Eng. Med. Biol. Soc. (EMBC)*, Milan, Italy, Aug. 2015, pp. 7606–7609.

[35] M. Piccardi, "Background subtraction techniques: A review," in *Proc. IEEE Int. Conf. Syst., Man Cybern.*, Hague, The Netherlands, Oct. 2004, pp. 3099–3104.

[36] J. Lai, Z. Yang, and B. Guo, "A two-stage low-complexity human sleep motion classification method using IR-UWB," *IEEE Sensors J.*, vol. 21, no. 18, pp. 20740–20749, Sep. 2021.